Simulations of a magnetically-shielded Hall effect thruster with conducting walls

IEPC-2024-571

J. Perales-Díaz [*] and E. Ahedo[†]

Department of Aerospace Engineering, Universidad Carlos III de Madrid, Madrid, Spain

and

A. Domínguez-Vázquez[‡]

Department of Mechanical, Thermal Engineering and Fluid Mechanics
Universidad de Málaga, Málaga, Spain

The discharge of a medium power, magnetically shielded Hall effect thruster with conducting channel walls is analyzed by means of numerical simulations with a two-dimensional axisymmetric hybrid PIC/fluid code. Two different electrical conditions for the conducting channel walls are considered: floating and anode-tied. The plasma discharges of these two scenarios are compared to each other and to the baseline case with ceramic dielectric channel walls. The main performance parameters and most of the bulk plasma properties are not significantly affected by the change in channel wall material and electrical condition. Main differences are found on the electron current density map inside the chamber for the anode-tied configuration. In this scenario, a different electron current distribution, shaped by the magnetic topology is found, the channel walls collecting up to a 75% of the discharge current. The lower electron current to the anode wall (53-54% relative decrease) reduces plasma power deposited there (32.5% relative decrease), which is beneficial from a thermal management point of view.

I.   Introduction

Future space missions demand the development of Hall effect thrusters (HETs) with reduced mass and production costs, as well as extended operation lifetimes.[1] The latter is achieved through the implementation of the magnetic shielding (MS) of the thruster channel walls, which practically eliminates wall erosion as a failure mode in HETs. Since MS topologies drastically reduce plasma-wall interaction, previous experimental studies have studied the possibility of replacing traditional dielectric channel walls made of ceramic material by conducting ones. Their goal is to achieve enhanced thruster operation and significant cost and mass savings, since conducting materials, in general, exhibit: (i) improved mechanical and thermomechanical properties with respect to ceramic materials and (ii) enhanced thermal conductivity and emissivity, which leads to a better thermal management and could allow increasing thruster power density.[1,2]

In particular, Goebel et al.[2] have considered graphite channel walls for the H6, 6 kW MS-HET, featuring a floating (i.e., electrically isolated) condition. With this configuration, they report only a slight reduction in the total thrust efficiency, η, with respect to the baseline configuration, with dielectric channel walls. At the same time, wall temperatures notably decrease, thanks to the enhanced thermal conductivity and emissivity, which increase heat dissipation from the thruster body. Consequently, they note that the use of conducting walls can pave the way to higher power density operation in HETs. Hofer et al.[1] have extended

---

[*]Postdoctoral researcher, Equipo de Propulsión Espacial y Plasmas (EP2), jperales@ing.uc3m.es
[†]Full Professor, Equipo de Propulsión Espacial y Plasmas (EP2), eahedo@ing.uc3m.es
[‡]Associate Professor, TEP-997, Equipo de Propulsión Espacial y Plasmas (EP2), adoming@uma.es.

the previous study to higher power and higher-than-nominal I_{sp} (up to 3000 s) operation, using graphite channel walls in the H9C, a 9 kW MS-HET. Apart from the floating channel wall scenario, Hofer et al. have tested conducting channel walls electrically connected to the anode (i.e., anode-tied configuration). Both set-ups are shown to be, in terms of performance, almost indistinguishable to the other, and to the dielectric channel wall configuration. Recently, conducting channel walls have enabled the demonstration of ultrahigh current density operation (10 times greater than nominal) in the H9C.[3] Grimaud et al.[4-6] have shown that the previous observations for high power-class MS-HETs also hold for low power-class ones. Therefore, MS-HETs with conducting channel walls are a promising and, seemingly, more suitable alternative to MS-HETs with conventional dielectric channel walls. However, how this switching from dielectric to conducting channel walls affects the plasma discharge is not yet fully understood.

In this work, numerical simulations of a MS-HET with conducting walls are carried out with HYPHEN, a 2D axisymmetric hybrid particle-in-cell(PIC)/fluid HET simulation code,[7-9] which has been recently upgraded for the simulation of advanced MS-HET prototypes.[10, 11] A 5 kW-class MS-HET virtual design, based on real MS-HET prototypes, featuring a centrally-mounted cathode and a magnetic null point inside the thruster chamber is studied here. Two different electrical configurations are considered for the conducting channel walls: floating and anode-tied. These are compared between each other and to the baseline case with dielectric channel walls in terms of performance, local plasma properties and power deposition to the walls.

The manuscript is structured as follows. Section II describes the virtural MS-HET thruster. Section III briefly introduces the HYPHEN simulation model. Then, the simulation set-up is presented in Section IV. Section V contains the simulation results and their discussion. Finally, the main conclusions are drawn in Section VI.

II.   Thruster description

The thruster considered for this numerical study, named VHET-MS, is a virtual 5 kW-class HET with MS topology designed by EP2 research group at Universidad Carlos III de Madrid (UC3M) as a benchmarking scenario for investigation purposes. Fig. 1(a) schematically shows the geometry of the VHET-MS. The annular chamber has a total length (including the chamfer) $L_c = 2.9$ cm and a radial extension (upstream the chamfer) $H_c = 2.22$ cm, extending from $r_{in} = 5.45$ cm to $r_{out} = 7.67$ cm. The anode placed on the chamber back wall is centered at $r_c = 6.56$ cm, and extends along the whole wall. The cathode is centrally-mounted, around the thruster chamber axis. The exit of the VHET-MS chamber is chamfered, as customarily in MS-HETs, to make the walls parallel to the local magnetic field, $\boldsymbol{B}$, streamlines.

Fig. 1(b) displays the $\boldsymbol{B}$ topology in both the plume region and the thruster chamber, while Fig. 1(c) presents a zoom of the thruster chamber, where $\boldsymbol{B}$ exhibits the characteristic shape of a MS topology.[12] Moreover, $\boldsymbol{B}$ features a null point (i.e., $B = 0$) in the middle of the channel. The B axial profile along the thruster channel midline is shown in Fig. 1(d). Along this line, the position of the $\boldsymbol{B}$ peak (~ 268 G) is located at $z/L_c \approx 1.2$, and the position of the $\boldsymbol{B}$ null point at $z/L_c \approx 0.49$. The magnitude of $\boldsymbol{B}$ at the anode is approximately 50 G.

III.   HYPHEN simulation model

HYPHEN is 2D axisymmetric code for simulating different plasma thruster discharges.[8, 13, 14] The HET version has been recently upgraded for MS prototypes with centrally-mounted cathodes.[10, 11] The code follows a hybrid formulation implemented modularly: the ion (I)-module includes a particle-in-cell (PIC) model to describe the dynamics of heavy species (neutrals and ions); the electron (E)-module solves a fluid model for the magnetized electrons. Quasineutrality is applied over the whole simulation domain and non-neutral effects are limited to planar Debye sheaths, which are treated as electrostatic discontinuities around the material boundaries of the domain, and solved by the S-module. The I-module operates on a structured mesh of the simulation domain (referred to as PIC mesh), shown in Fig. 2(a). On the contrary, to limit numerical diffusion associated to the strong anisotropic transport of magnetized electrons, the E-module operates on an unstructured magnetic field aligned mesh (MFAM),[15] depicted in Fig. 2(b), whose inner cells are defined by local $\boldsymbol{B}$-parallel and perpendicular lines [streamlines (blue) and equipotential lines (red) in Fig. 2(b)] obtained from the externally applied (solenoidal and irrotational) $\boldsymbol{B}$.

Every simulation step, the I-module takes as inputs $\boldsymbol{B}$; the electric field, $\boldsymbol{E}$; and the electron temper-
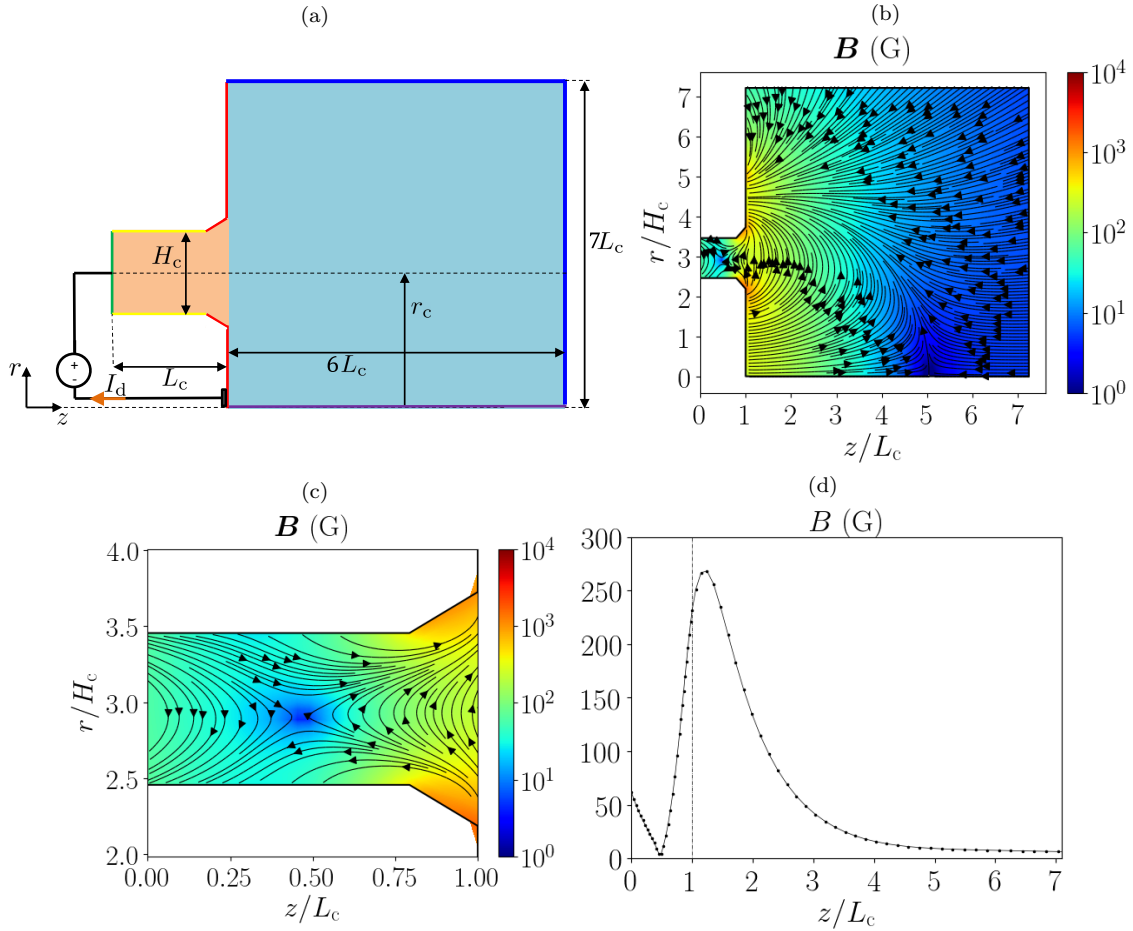
Figure 1. (a) Sketch of the VHET-MS, (b) B topology, (c) B topology within the thruster chamber, and (d) magnitude of B along the thruster chamber midline. Black lines with arrows in (b) and (c) are B streamlines.

ature, T_e; and performs the following tasks: (i) ion and neutral macroparticle propagation; (ii) injection and removal of macroparticles from/to simulation boundaries; (iii) macroparticle-wall interactions including neutral reflection and ion recombination; (iv) generation of new ion macroparticles from ionization; and (v) computation of the heavy species macroscopic properties through particle-to-mesh weighting algorithms, including: the neutral density, n_n; the plasma density, n_e; and the ion current density vector, j_i. The E-module, taking these heavy-species macroscopic magnitudes as inputs, solves a quasineutral, drift-diffusive (inertialess) fluid model for the magnetized electron population, obtaining the electric potential, ϕ; the electron temperature, T_e; the electron current density vector j_e; and the electron heat flux vector q_e. A Fourier-like closure for q_e is considered. For a detailed description of the numerical treatment of the electron fluid equations in HYPHEN, the reader is referred to the work of Zhou et al.[14] Electron turbulent transport is modeled through an anomalous collision frequency $\nu_t = \alpha_t \omega_{ce}$, with $\omega_{ce} = eB/m_e$ the electron gyrofrequency and $\alpha_t(z)$ an empirical turbulence level function that is tuned to match time-averaged experimental data as the discharge current, I_d, and the thrust, F. Here, a step-out function is considered, featuring two parameters, α_{t1} and $\alpha_{t2}(> \alpha_{t1})$, applied, approximately, in the thruster chamber and in the near plume, respectively, which are fitted to reproduce data on I_d and F. This calibration strategy has been successfully used in previous numerical studies of MS-HETs.[10]

The reference $\phi = 0$ for the potential is set at the cathode boundary faces, so the anode potential is V_d. The simulation domain extends up to the sheath edge (Q) of the quasineutral plasma, represented by the MFAM boundary faces. Depending on the type of wall (W) (i.e. conducting or dielectric), the S-module provides the appropriate boundary conditions at each MFAM boundary face in the form of nonlinear relations for $j_{ne} = \mathbf{1}_n \cdot j_e$ and $q_{ne} = \mathbf{1}_n \cdot q_e$, with $\mathbf{1}_n$ being the *outward* unit normal vector (expressions are detailed in the Appendix of Ref. 10 and omitted here), as a function of the electric potential jump across the

sheath $\Delta\phi_{\mathrm{WQ}} = \phi_{\mathrm{Q}} - \phi_{\mathrm{W}}$. The sheath model includes elastically reflected electrons and secondary electron emission (SEE) from the dielectric walls, and also retains other non-Maxwellian features of the electron velocity distribution function, such as the replenishment fraction of its high energy tails.[16] At a dielectric wall $j_{\mathrm{ne}} = -j_{\mathrm{ni}}$ is imposed, providing $\Delta\phi_{\mathrm{WQ}}$. At a current-driving conducting wall at known potential ϕ_{W} (i.e., anode or anode-tied conducting channel walls here at $\phi_{\mathrm{W}} = V_{\mathrm{d}}$), the nonlinear function $j_{\mathrm{ne}}(\Delta\phi_{\mathrm{WQ}})$ is linearized and solved iteratively to ensure current continuity (refer to Ref. 10 for further details). At floating conducting walls, a similar procedure is followed, solving for the wall floating potential ϕ_{W} that ensures null net current collected by the wall (i.e. $I_{\mathrm{W}} = 0$). At the cathode boundary faces, the electron injected current density ($j_{\mathrm{ne}} > 0$) is defined by I_{d} divided by the cathode wall surface. The electron energy flux at each cathode face, expressed as $q_{\mathrm{ne}} = -5T_{\mathrm{e}}j_{\mathrm{ne}}/(2e)$, is set equal to $-2T_{\mathrm{C}}j_{\mathrm{ne}}/e$, with $2T_{\mathrm{C}}$ being the average emission energy per electron. At the plume downstream boundary P a global downstream matching layer (GDML) model for the off-simulation region, summarizing the electron dynamics in the infinite plume expansion is applied here.[17] The GDML model is defined as a thin boundary layer that provides expressions for j_{ne} and q_{ne} and permits to estimate the final potential in the plume ϕ_∞ for a globally current free plume (i.e. $I_{\mathrm{P}} = 0$).

IV. Simulation setup

The set-up for the VHET-MS simulations is presented in this section. The extension of the simulation domain is about $7L_{\mathrm{c}}$ ($6L_{\mathrm{c}}$ for the plume region) in the axial direction and $7H_{\mathrm{c}}$ in the radial direction [refer to Fig. 1(a)]. Figs. 2(a) and 2(b) shows the PIC mesh and the MFAM, respectively, for the simulation of the VHET-MS discharge. The relevant characteristics of the meshes and simulation parameters are listed in Tab. 1. The green line at the left boundary in Fig. 2(a) indicates the position of the annular anode wall and the small black box represents the centrally-mounted cathode. The red lines, covering the chamfer and the radially-extending lateral walls of the thruster, correspond to dielectric walls. The magenta line identifies the symmetry axis and the blue lines the downstream plume boundary P. The yellow lines represent the thruster channel walls, whose material and electrical properties are modified in the present study. In particular, a dielectric material (boron nitride), and a conducting one in floating and anode-tied conditions are considered here. In the floating wall scenario, the inner and outer channel walls are electrically independent to each other. At boron nitride dielectric walls, empirical parameters for plasma-wall interaction, including SEE, are taken as in previous numerical studies of real MS-HET prototypes.[10] Conducting walls feature no SEE here. The sensitivity of the simulation results to these walls parameters has been proven small, due to the MS configuration of the thruster.[11] Fig. 2(c) details the magnetic topology in the thruster chamber, showing the location of the magnetic null point ($B = 0$), where magnetic streamlines (blue lines) and magnetic isopotential lines (red lines) intersect. The small black box in Figs. 2(a) and (b) represents the central cathode, which is modeled as a surface boundary.

A given mass flow rate of Xe neutrals $\dot{m}_{\mathrm{A}}$ is injected into the simulation domain from a Maxwellian reservoir through the whole anode wall. The injection is performed uniformly along the anode surface with a given temperature[18] and sonic drift velocity (see Tab. 1). Considering the same injection conditions, a neutral mass flow, $\dot{m}_{\mathrm{C}} = 0.075\dot{m}_{\mathrm{A}}$, is injected through the cathode surface. Therefore, the total injected propellant mass flow is $\dot{m} = \dot{m}_{\mathrm{A}} + \dot{m}_{\mathrm{C}}$. Cathode electrons are emitted with an energy $2T_{\mathrm{C}} = 4.5\mathrm{eV}$.[19] The injected neutrals are ionized, upon collision with electrons, into singly and doubly-charged ions inside the simulation volume. The ionization rate data are taken from the BIAGI database,[20] for single ionization rates, and the Drawin model,[21] for double ionization rates, including the ionization events $A + e \rightarrow A^{++} + 3e$, and $A^+ + e \rightarrow A^{++} + 2e$. Ion macroparticles undergo recombination into neutrals at any material wall. In this process, neutrals are reinjected diffusely, imposing complete energy accomodation, (i.e., with the temperature of the walls, which is set to 850K[18]). Moreover, neutral macroparticles experience diffuse reflection at the walls with zero energy accommodation (see previous works with HYPHEN[8,22] for further details). The algorithm for macroparticle population control is activated, with a target of 100 macroparticles per cell of each heavy-species population, with a $\pm 10\%$ of tolerance.[8]

The (ion) timestep is set in such a way that the fastest doubly-charged ion takes, as minimum, two timesteps to cross the smallest cell of the PIC mesh (see Tab. 1). Simulations are started considering only neutrals, injected from anode and cathode, to quickly fill the simulation domain. Then, the full simulation starts with an initial background plasma density to spark the discharge.[22] The number of simulated timesteps is 60000 (900 μs of simulation time), enough to capture several low-frequency (i.e. breathing mode) oscillation

4

The 38th International Electric Propulsion Conference, P. Baudis Convention Center, Toulouse, France, June 23-28, 2024
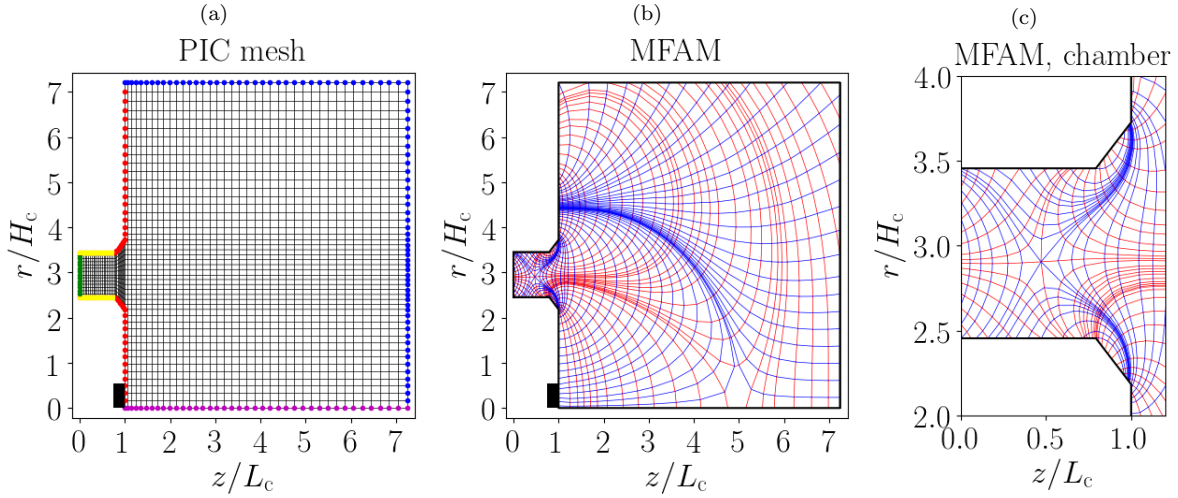
Figure 2. (a) Structured PIC mesh (b) MFAM. (c) Detail of the MFAM within the thruster chamber. In (a), the boundary type is identified by its color: in green the anode wall; in yellow the channel walls (i.e. dielectric or conducting); in red the dielectric walls; in blue the downstream plume boundary, P. Blue and red lines in (b) and (c) are B-parallel and B-perpendicular lines, respectively.

Table 1. Main simulation parameters and mesh characteristics.

Simulation parameter	Units	Value
PIC mesh number of cells, nodes	-	3243, 3360
PIC mesh smallest grid size	mm	1
MFAM number of cells, faces	-	2030, 4171
MFAM average skewness[23]	-	0.059
Ion-moving timestep, Δt	ns	15
Total number of simulation steps	-	60000
Injected Xe velocity	ms^{-1}	300
Injected Xe temperature	K	850

cycles of I_{d}. The results presented in the following sections are time-averaged over a given number of several I_{d} oscillation cycles.

The first three columns of Tab. 2 lists the input parameters that characterize the VHET-MS operation point considered for this study, which are kept the same for the three simulated cases here. These simulation cases are labeled as follows: Case D for the dielectric channel wall scenario, Case C-Float for the scenario with floating conducting channel walls, and Case C-Tied for scenario with anode-tied conducting channel walls. The operation point considered is within the range of nominal operative conditions for a 5 kW-class HET, and it coincides with the reference case of a previous numerical study in Perales-Díaz et al.,[10] on SITAEL's HT5k thruster. The fitting of the anomalous transport model takes as baseline that of Perales-Díaz et al.,[10] with slight modifications in the parameters $\alpha_{\mathrm{t}1}(=0.4\%)$ and $\alpha_{\mathrm{t}2}(=4\%)$ to achieve values of I_{d} and F similar to those of the HT5k for the considered operation point. The anomalous transport parameters are kept the same for the three simulation cases presented here.

V. Results

A. Plasma bulk analysis

Figure 3 presents the time-averaged 2D maps inside the thruster chamber of relevant plasma variables of the VHET-MS discharge for (left column) Case D, (middle column) Case C-Float and (right column) Case C-Tied. Focusing firstly on the baseline scenario Case D, its 2D contours exhibit the usual features of a

Table 2. Definition of the simulated operation point in terms of: anodic mass flow rate, $\dot{m}_A$, cathode mass flow rate, $\dot{m}_C$, discharge voltage, V_d. Values of the main performance metrics: I_d, F, P and η.

V_d (V)	$\dot{m}_A$ (mg/s)	$\dot{m}_C$ (mg/s)	I_d (A)	F (mN)	P (kW)	η (%)	
			14.0	257	4.22	52.0	Case D
300	14	1.05	13.9	255	4.18	51.6	Case C-Float
			14.0	255	4.19	51.7	Case C-Tied

MS-HET plasma discharge:[10, 24] the outward displacement of the acceleration region, in Fig. 3(g) and the consequent relative uniformity of ϕ (with values close to the anode potential $V_d = 300$ V) and n_e, in Figs. 3(g) and (d), respectively; and the low T_e along the thruster chamber walls, in Fig. 3(j). Figure 3(a) shows that n_n decreases by about 2 orders of magnitude within the thruster chamber, indicating high propellant utilization, and in line with the relatively high n_e. Figure 4 shows the 1D axial profiles along the thruster chamber midline of n_n, n_e, ϕ, T_e and the magnitude of the longitudinal (i.e. axial and radial components only) ion and electron current density vectors, $\tilde{\boldsymbol{j}}_i$ and $\tilde{\boldsymbol{j}}_e$, respectively. The plots in the left column show profiles within the thruster chamber, while the plots in the right column correspond to the axial profiles along the complete simulation domain. Figure 4(b) reveals the axial increase of n_n in the plume, due to the merging of the neutrals coming from the thruster chamber and those injected from the central cathode. Moreover, as observed in the simulations of the HT5k thruster,[10] most of the axial ϕ fall takes place in a distance of around $2L_c$ [see Fig. 4(f)]. T_e peak (of about 45 eV) is located outside the thruster chamber, close to the B peak [refer to Fig. 2(d)] and the $E_z \equiv -\partial\phi/\partial z$ peak (not shown).

Figures 3 and 4 show a similar solution for n_n, n_e, T_e for all cases. Only ϕ in Case C-Tied exhibits a small increase with respect to the other two cases (in line with the fact that conducting channel walls are set at $V_d = 300$ V), but the gradients seem to change only slightly. The similar solution for n_n, n_e, ϕ and T_e among the three simulated cases (also downstream the thruster chamber exit), is in line with the fact that overall performance figures as I_d, F, the input power P and the thrust efficiency, defined as

$$\eta = \frac{F^2}{2\dot{m}P},\tag{1}$$

are barely affected by the change in the material properties (and electrical connection) of the channel walls (see Tab. 2), in agreement with the previous experimental works.[1, 2, 4]

On the other hand, the solution of $\tilde{\boldsymbol{j}}_i$ and, especially, $\tilde{\boldsymbol{j}}_e$, exhibit larger differences across the simulated cases. In Fig. 4(i), $\tilde{\jmath}_i$ increases close to the anode for Case C-Tied (see Sec. C for further details). Figure 4(k) shows that $\tilde{\jmath}_e$ for Case C-Tied is significantly lower than for Cases D and C-Float in the region extending from the anode wall to $z/L_c \approx 0.5$, where $\tilde{\jmath}_e$ peaks along the thruster channel midline. Interestingly, for all cases $\tilde{\jmath}_e$ peaks close to the B null point, which seems to axially split the simulation domain into a downstream region, where all cases exhibit the same $\tilde{\jmath}_e$ profile, and an upstream region where Case C-Tied exhibits a different $\tilde{\jmath}_e$ solution.

Figure 5 depicts the 2D vector maps (magnitude and streamlines) of $\tilde{\boldsymbol{j}}_e$ (first row), $\tilde{\boldsymbol{j}}_i$ (second row) and $\tilde{\boldsymbol{j}}$ (third row) for Case D, C-Float and C-Tied in columns from left to right, respectively. Figures 5(d)-(f) show a similar $\tilde{\boldsymbol{j}}_i$ solution for all cases, the ion streamlines reflecting the existence of backward, forward, and lateral ion flows. Although there is a point with $\tilde{\boldsymbol{j}}_i = 0$, located at $z/L_c \sim 0.3$, notice that the ionization source is distributed in the whole channel volume and the streamlines represent the ion macroscopic behavior. Ions are practically unmagnetized, follow the local the electric field and are not prevented from impacting the thurster chamber walls. For all cases, similar ion currents are collected by the different walls, as detailed in Sec. C, in line with the similar ϕ and n_e solution within the chamber.

Figures 5(a) and (b) reveal similar $\tilde{\boldsymbol{j}}_e$ maps (in both magnitude and direction) between Cases D and C-Float in the plasma bulk, due to the fact that in both cases the net electric current collected at the conducting channel walls is null. The lateral cusped B structures of the MS topology channel most of the electron flow towards the anode wall. The net electron current collected at the lateral channel walls is practically the same in both cases (see later in Sec. C). The null local current condition imposed at the dielectric channel walls in Case D yields $\tilde{\boldsymbol{j}}$ streamlines parallel to the walls in Fig. 5(g). On the other hand, the floating condition in Case C-Float permits electric current density to flow locally from plasma to the
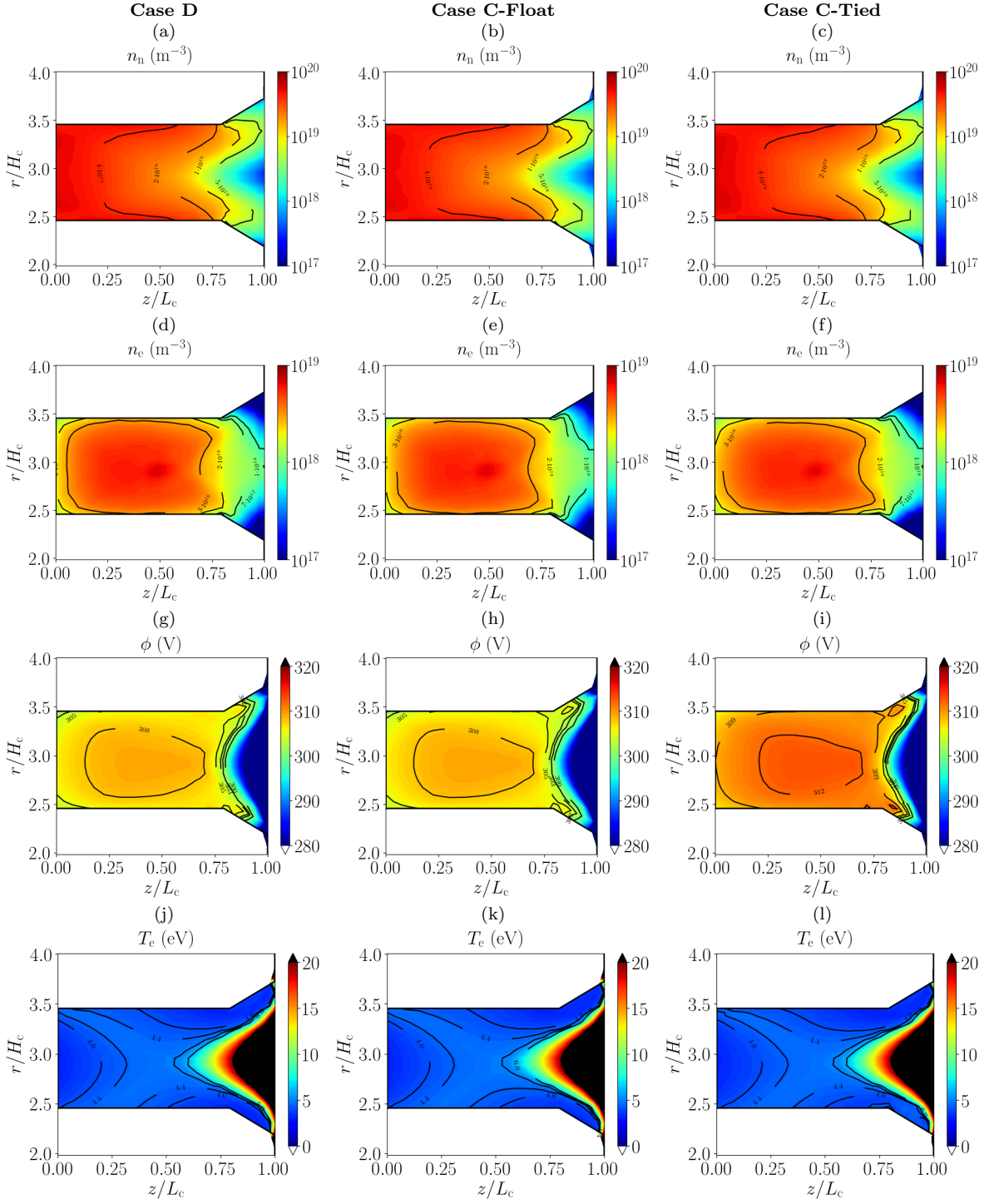
Figure 3. **Time-averaged 2D(z,r) contour maps inside the thruster chamber for cases with (left column) dielectric, (middle column) floating conducting, and (right column) anode-tied conducting channel walls. (a)-(c) Neutral density n_n, (d)-(f) plasma density n_e, (g)-(i) electric potential ϕ and (j)-(l) electron temperature T_e.**

channel walls and vice versa, with $\tilde{\boldsymbol{j}}$ locally intersecting channel walls in the corresponding directions [refer to 5(h)], so that the net current collected is null.

Upstream the $\boldsymbol{B}$ null point, Case C-Tied exhibits a notably different $\tilde{\boldsymbol{j}}_\mathrm{e}$ magnitude map with respect to Cases D and C-Float, as depicted in Fig. 5(c). Differences are induced by the change in the boundary
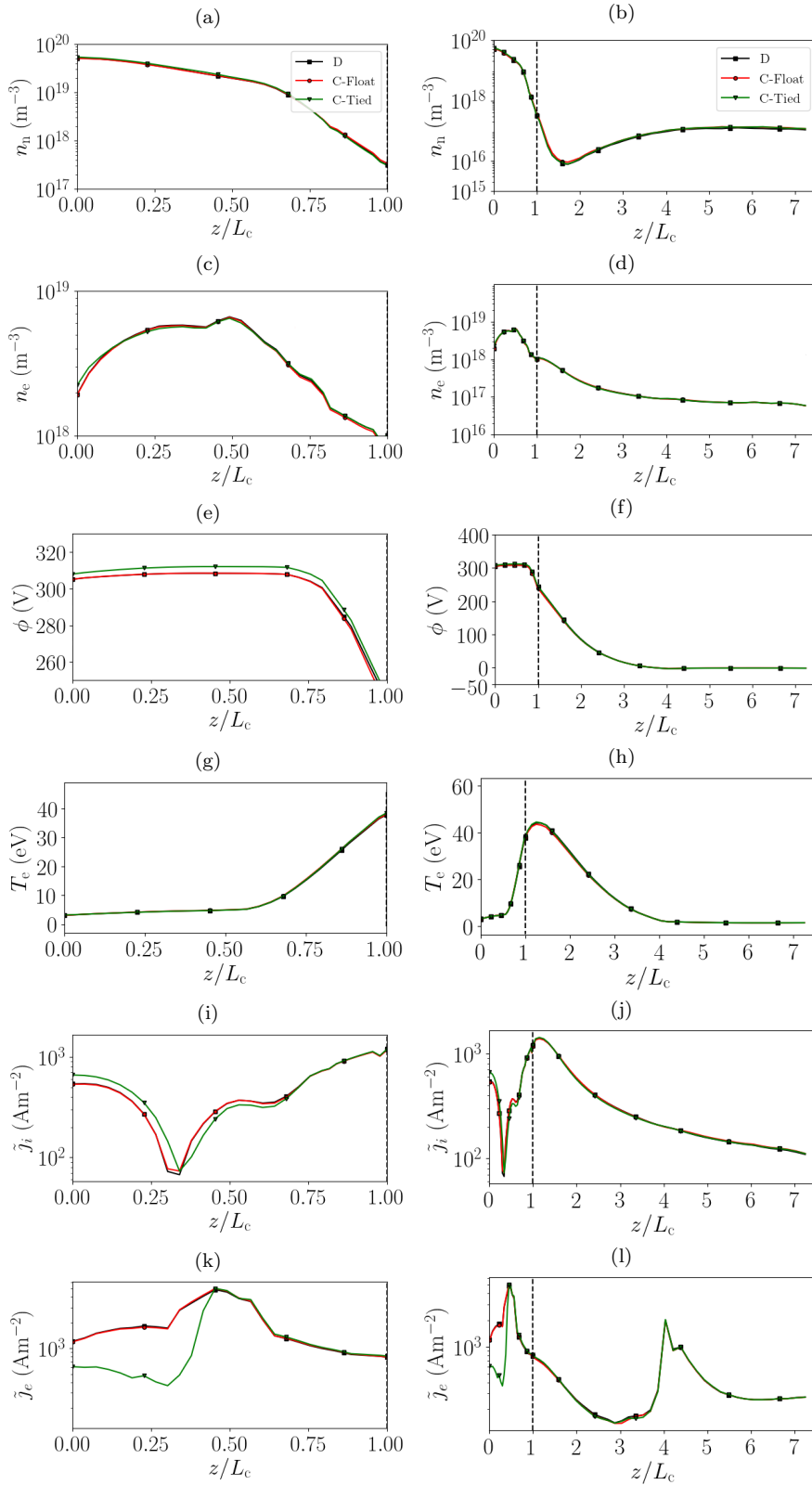
Figure 4. Time-averaged 1D axial profiles along the thruster chamber midline for Case D (in black), C-Float (in red) and C-Tied (in green) of (a)-(b) n_n, (c)-(d) n_e, (e)-(f) ϕ, (g)-(h) T_e, and magnitude of (i)-(j) $\tilde{j}_i$ and (k-l) $\tilde{j}_e$. Magnitudes inside the chamber (left column), and along the whole simulation domain (right column).
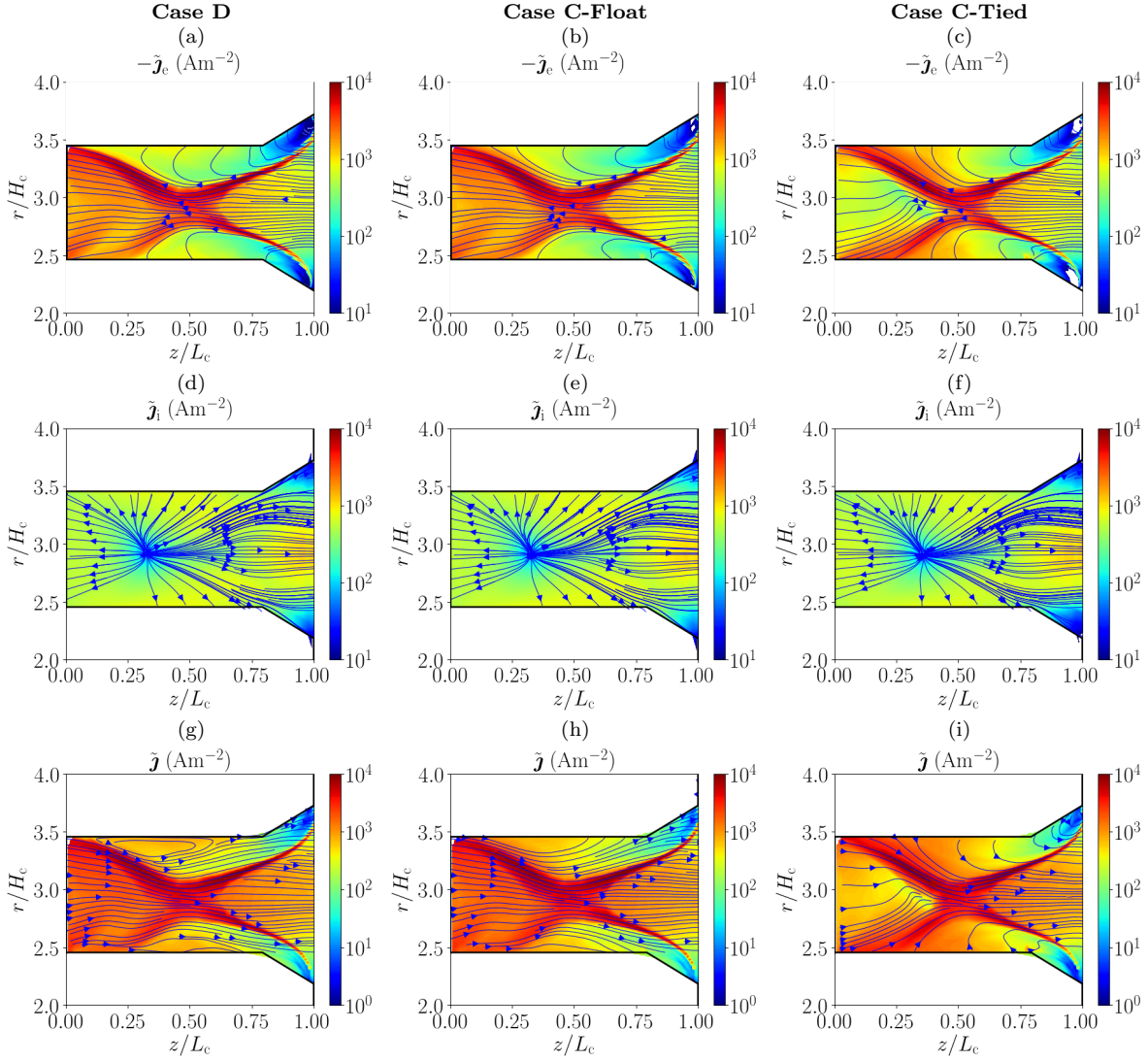
Figure 5. Time-averaged 2D(z,r) contour maps inside the thruster chamber of the magnitude of (a)-(c) $\tilde{\boldsymbol{j}}_e$, (d)-(e) $\tilde{\boldsymbol{j}}_i$ and (g)-(i) $\tilde{\boldsymbol{j}}$ for Case D (first column), C-Float (second column) and C-Tied (third column). Blue lines with arrows indicate streamlines of $-\tilde{\boldsymbol{j}}_e$, $\tilde{\boldsymbol{j}}_i$ and $\tilde{\boldsymbol{j}}$, respectively.

condition imposed at the channel walls: unlike in Cases D and C-Float, the anode-tied conducting channel walls in Case C-Tied can collect a certain net electric current (i.e., a fraction of I_d), thus decoupling net ion and electron currents collected at the channel walls. While the unmagnetized ion current solution is practically unafected, $\boldsymbol{B}$ topology shapes the magnetized electrons current map, and a large fraction of electrons are directed towards the lateral channel walls along $\boldsymbol{B}$ lines born from the magnetic null point [refer to Figs. 1(c) and 2(c)], where electrons are unmagnetized and can easily move across magnetic tubes. These electrons are collected where these $\boldsymbol{B}$ lines impinge the channel walls, close to the anode, coinciding with the region of higher T_e [see Fig. 3(l)], and thus weaker MS, of the walls. Current streamlines from the lateral channel walls into the domain in this region indicate that the net current collected by the channel walls is mainly driven by electrons (as for the anode wall), and contributes to a ~75% of I_d (see later in Sec. C). Since I_d is the same for all cases, this fact explains the lower magnitude of $\tilde{\boldsymbol{j}}_e$ (and $\tilde{\boldsymbol{j}}$) in case C-Tied in the near-anode region upstream the magnetic null point [refer to Figs. 4(k)-(l), 5(c) and 5(i)].

These results for Case C-Tied highlight the central role of the B topology and, in particular, the presence and location of the magnetic null point in the electron current solution in the chamber. Near the magnetic singularity, electrons can easily cross magnetic lines and, therefore, $\tilde{\boldsymbol{j}}_e$ can be redistributed from there (according to the different electrical conditions of the channel walls) without a significant change in ϕ and

n_e gradients. Effects over the plasma solution of the presence and position of the $\boldsymbol{B}$ null point deserves particular attention, and is left for further research.

B. Wall profiles

Fig. 6 shows the profiles along the thruster chamber walls of relevant plasma variables. The abscissa length coordinate s starts ($s = 0$) at the outermost end of the inner channel wall and runs over the inner channel wall [yellow inner boundary in Fig. 2(a)], the anode wall [green boundary in Fig. 2(a)] and the outer channel wall [yellow outer boundary in Fig. 2(a)]. In Fig. 6(a), the thruster channel wall potential ϕ_W changes only a few volts (< 5 V) along the wall in Cases D (black) and C-Float (red). In Case C-Float (red line), ϕ_W at each channel wall adapts to collect a null electric current. This characteristic makes the anode profiles of all plasma magnitudes of Case C-Float (red lines) perfectly match those of Case D (black lines). The inner and outer channel walls in Case C-Float exhibit very similar ϕ_W, due to the nearly-symmetric $\boldsymbol{B}$ inside the thruster chamber with respect to the channel midline. Fig. 6(b) shows that Case C-Float is the one with the largest sheath potential drop, $\Delta\phi_{WQ}$, along the channel walls, in order to locally regulate the electron flux and ensure null total electric current collected. On the other hand, Case C-Tied exhibits a more uniform $\Delta\phi_{WQ}$ profile along the chamber walls, with closer values at the anode and channel walls, which act as an "extended-anode" in this configuration. Results for ϕ_W and $\Delta\phi_{WQ}$ indicates that MS is effective in keeping nearly constant ϕ values, close to V_d, around the thruster chamber walls for all cases analyzed here.

Figures 6(c) and (d) show the energy deposited on the wall per average impacting ion particle (i.e., accounting for singly and doubly-charged ions), $\mathcal{E}_{i,wall}$ and per net collected electron, $\mathcal{E}_{e,wall}$. In Fig. 6(c), the differences among $\mathcal{E}_{i,wall}$ profiles are mostly determined by changes in $\Delta\phi_{WQ}$ [in Fig. 6(b)], since the gradients of ϕ within the plasma bulk barely change from one case to the other [see Figs. 3(g)-(i)]. Comparing among configurations, Case C-Tied exhibit the largest $\mathcal{E}_{i,wall}$ at the anode wall, while Case C-Float does so at the channel walls. In all cases, $\mathcal{E}_{i,wall}$ is well below typical erosion thresholds,[25,26] since MS remains effective in keeping low T_e [see Figs. 3(j)-(l)] values and nearly constant ϕ around thruster chamber walls. In Fig. 6(d), $\mathcal{E}_{e,wall}$ is a function of the local T_e and the SEE yield, δ_s.[10] On the one hand, T_e along the wall [see Fig. 3(j)-(l)] does not vary across the different cases, because the T_e distribution inside the thruster chamber is essentially determined by the magnetic field topology. On the other hand, δ_s is zero everywhere for Cases C-Float and C-Tied, while $\delta_s \approx 0.15$ along the channel walls in Case D. Due to this small fraction of SEE, $\mathcal{E}_{e,wall}$ is slightly larger in the channel walls in Case D.

Figures 6(e) and (f) show, respectively, j_n, and j_{ni} and j_{ne} In Fig. 6(f), j_{ni} slightly change across the different cases. In Case D, the dielectric condition makes j_{ni} and j_{ne} locally equal (and thus $j_n = 0$) along the channel walls. In Case C-Float, instead, although the total collected electric current at the channel walls is null, j_{ne} is not locally equal to j_{ni}, and therefore, j_n is different from zero along this surface, switching from positive (along the outermost segment) to negative values (close to the anode). For Cases D and C-Float, at the anode wall j_{ne}, exhibit the same profile and is larger than j_{ni}. On the other hand, Case C-Tied exhibits a significantly different j_{ne} profile along walls, with larger j_{ne} values at the channel walls and lower at the anode one (which is even lower than j_{ni} in the central part of the anode wall). Since ϕ_W at the channel walls for Case C-Tied (= 300 V) is higher than ϕ_W for Case C-Float (≈ 293 V), we find $j_n < 0$ (i.e., electric current is electron dominated) along most of the anode-tied channel wall, and j_{ne} (and j_n) are lower at the anode wall, as observed in Figs. 6(e) and (f). These results are in line with the discussion on $\tilde{\boldsymbol{j}}_e$ solution in Sec. A.

Figures 6(g) and (h) show the plasma energy flux to the walls, P''_n, and the contributions from ions, P''_{ni}, and electrons, P''_{ne}. For Case D and C-Float, since $\mathcal{E}_{e,wall} < \mathcal{E}_{i,wall}$ and ion and electron currents are similar (or equal), we find $P''_{ne} < P''_{ni}$ along most of the channel walls. At the anode wall, the larger j_{ne} yields $P''_{ne} > P''_{ni}$, since ion and electron impact energies are similar. For Case C-Tied, the P''_{ne} profile nearly follows the j_{ne} profile: it increases at the channel walls and decreases at the anode wall. As for ions, the opposite behavior is found, and P''_{ni} decreases at the channel walls and increases at the anode wall. As a result, a more uniform plasma power deposition profile is obtained, with lower maxima than in Cases D and C-Float, and located at the channel walls, instead of at the anode.

C. Current and power balances

HYPHEN is able to compute the currents and energy fluxes collected by the different boundaries of the simulation domain. This allows us to pose current and power balance equations, for the sake of a performance
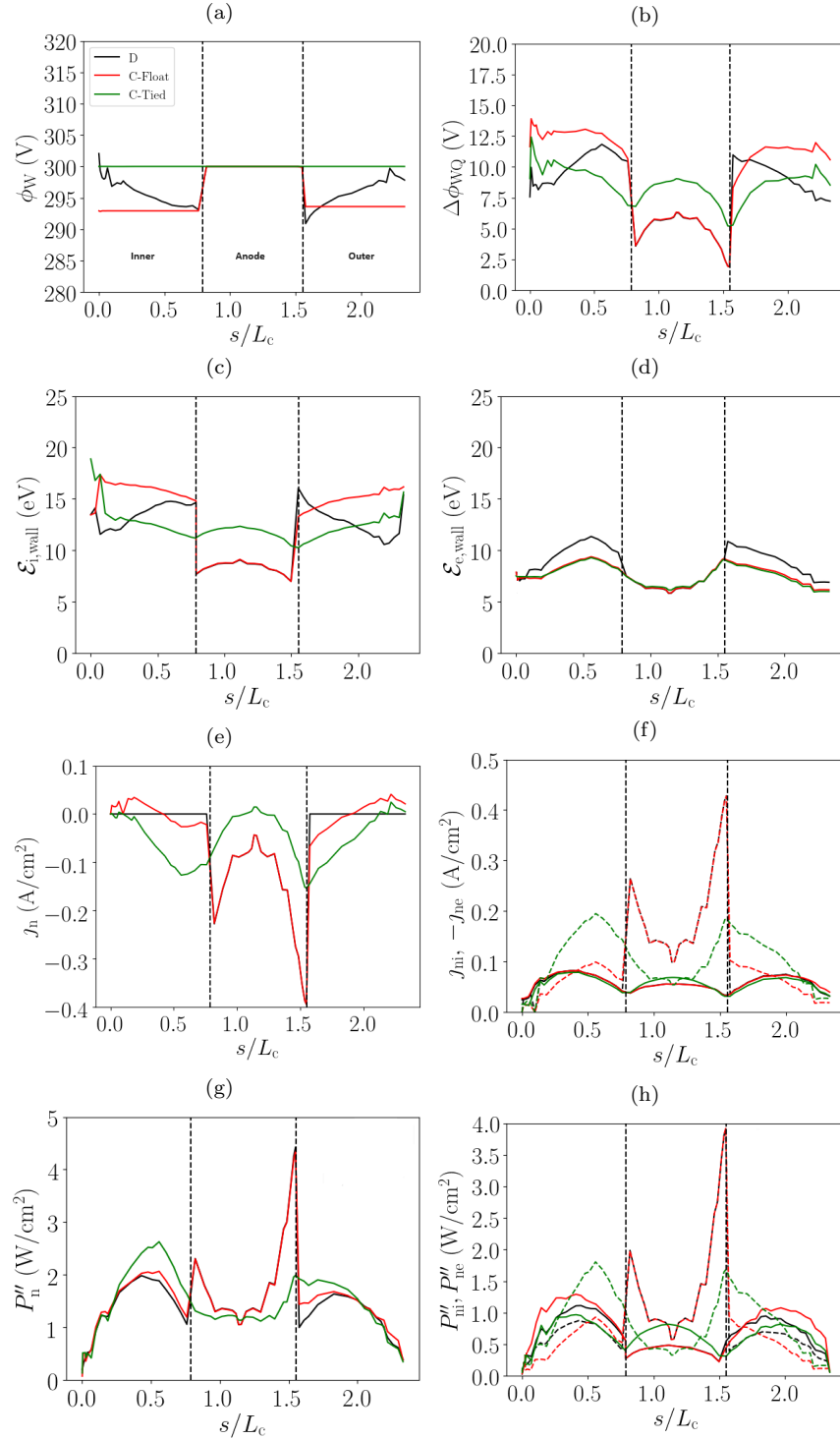
Figure 6. Time-averaged 1D profiles along the thruster channel walls [yellow boundaries in Fig. 2(a)] for Case D (black lines), Case C-Float (red lines) and Case C-Tied (green lines). Coordinate s runs from the outermost end of the inner channel wall to the outermost end of the outer channel wall. Profiles of (a) electric potential at the wall, ϕ_{W}; (b) sheath potential fall, $\Delta\phi_{\mathrm{WQ}}$; (c) ion wall-impact energy, $\mathcal{E}_{\mathrm{i,wall}}$; (d) electron wall-impact energy, $\mathcal{E}_{\mathrm{e,wall}}$; (e) electric current normal to the walls, j_{n}; (f) ion (solid line) and electron (dashed line) currents normal to the walls, j_{ni}, and $-j_{\mathrm{ne}}$, respectively; (g) total power deposition per unit surface, P_{n}''; and (h) ion (solid line) and electron (dashed line) power deposition per unit surface, P_{ni}'' and P_{ne}'', respectively.

Table 3. Terms of the ion and electron current balances, according to Eqs. (2) and (3); and current-related partial efficiencies.

Case	I_{prod} (A)	I_{d} (A)	$I_{\mathrm{W}}/I_{\mathrm{d}}$ (%)	$I_{\mathrm{iW}}/I_{\mathrm{prod}}$ (%)	$I_{\mathrm{iA}}/I_{\mathrm{prod}}$ (%)	$I_{\mathrm{iP}}/I_{\mathrm{prod}}$ (%)	$I_{\mathrm{eW}}/I_{\mathrm{prod}}$ (%)	$I_{\mathrm{eA}}/I_{\mathrm{prod}}$ (%)	$I_{\mathrm{eP}}/I_{\mathrm{prod}}$ (%)	η_{u} (%)	η_{cur} (%)	η_{ch} (%)
D	28.6	14.0	0.0	44.2	14.3	41.2	44.2	64.0	41.2	92.6	83.6	87.0
C-Float	28.6	13.9	0.0	44.8	14.0	40.9	44.8	62.9	40.9	92.3	83.8	87.4
C-Tied	28.1	14.0	75.1	41.6	16.6	41.5	79.0	29.3	41.5	91.9	83.6	87.0

analysis of the thruster discharge. In the particular set-up considered for the present study, the time-averaged balance on ion currents can be expressed as:

$$I_{\mathrm{prod}} = I_{\mathrm{iP}} + I_{\mathrm{iW}} + I_{\mathrm{iA}} + I_{\mathrm{iC}}, \tag{2}$$

where I_{prod} is the total ion current generated by ionization in the simulation domain; I_{iW} is the ion current collected at the thruster walls other than the anode [i.e., the yellow and red walls in Fig. 1(a)]; I_{iA} is the ion current collected at the anode wall [green wall in Fig. 1(a)]; and I_{iP} is the ion beam current leaving the domain across the plume boundary [in blue in Fig. 1(a)]. The term I_{iW} is completely dominated by the channel walls contribution (yellow boundary), being residual ($< 1\%$) the contribution from the dielectric walls (red boundary). Similarly, the electron current balance can be defined as, with identical meaning of the subscripts:

$$I_{\mathrm{prod}} + I_{\mathrm{eC}} = I_{\mathrm{eP}} + I_{\mathrm{eW}} + I_{\mathrm{eA}} \tag{3}$$

where all currents are considered positive and $I_{\mathrm{d}} = I_{\mathrm{A}} + I_{\mathrm{W}} = I_{\mathrm{eC}} + I_{\mathrm{iC}}$, with $I_{\mathrm{A}} = I_{\mathrm{eA}} - I_{\mathrm{iA}}$ the net current collected at the anode wall and $I_{\mathrm{W}} = I_{\mathrm{eW}} - I_{\mathrm{iW}}$ the net current collected at the channel walls (only different from zero for Case C-Tied here). The propellant utilization, current and charge efficiencies are defined, respectively, as

$$\eta_{\mathrm{u}} = \frac{\dot{m}_{\mathrm{iP}}}{\dot{m}}, \qquad \eta_{\mathrm{cur}} = \frac{I_{\mathrm{iP}}}{I_{\mathrm{d}}}, \qquad \eta_{\mathrm{ch}} = \frac{e\dot{m}_{\mathrm{iP}}}{m_{\mathrm{i}} I_{\mathrm{iP}}}, \tag{4}$$

where $\dot{m}_{\mathrm{iP}}$ is the mass flow of ions crossing the plume boundary, e the elementary charge and m_{i} the propellant atomic mass.

The time-averaged power balance is

$$P = P_{\mathrm{P}} + P_{\mathrm{W}} + P_{\mathrm{A}} + P_{\mathrm{inel}}, \tag{5}$$

where $P = I_{\mathrm{d}} V_{\mathrm{d}} + P_{\mathrm{C}}$ is the input power, which includes a tiny ($\sim 1\%$) contribution, P_{C}, from the electron injection at the cathode; P_{P} is the flow of plasma energy across the plume boundary; P_{W} and P_{A} represent plasma energy flows on, respectively, the thruster walls (other than the anode) and the anode wall; and P_{inel} is the energy loss due to inelastic (ionization and excitation) collisions on the whole simulation domain. P_{W} is dominated by the contribution from the channel walls [yellow boundary in Fig. 2(a)].

The thrust efficiency in Eq. (1) is factorized as

$$\eta = \eta_{\mathrm{ene}} \eta_{\mathrm{div}} \eta_{\mathrm{disp}}, \tag{6}$$

where η_{ene}, η_{div} and η_{disp} correspond to energy, plume divergence, and velocity dispersion efficiencies defined, respectively, as

$$\eta_{\mathrm{ene}} = \frac{P_{\mathrm{P}}}{P}, \qquad \eta_{\mathrm{div}} = \frac{P_{\mathrm{zP}}}{P_{\mathrm{P}}}, \qquad \eta_{\mathrm{disp}} = \frac{F^2}{2\dot{m} P_{\mathrm{zP}}}, \tag{7}$$

with P_{zP} the flow of axial plasma energy through the plume boundary. η_{div} assesses the plume divergence based on axial energy and total energy flows, and η_{disp} quantifies the level of velocity dispersion of all plasma species (which would be one for a beam constituted of mono-velocity particles).

Tables 3 and 4 present the relative contributions to the current and power balances, respectively, as defined in Eqs. (2), (3) and (5), and their related partial efficiencies. Ion and electron currents and powers at the thruster walls (subscripts W and A) are obtained from surface integrals of j_{ni}, $-j_{\mathrm{ne}}$, P''_{ni} and P''_{ne}, in Figs. 6(f) and (h), respectively, at corresponding walls. In Tab. 3, the electron current balance contributions are normalized with I_{prod} (instead of $I_{\mathrm{prod}} + I_{\mathrm{eC}}$) for a direct comparison to ion current balance contributions.

Table 4. Terms of the power balance, with separated ion and electron contributions, according to Eq. (5), and related partial efficiencies and total efficiency.

Case	P (kW)	P_{inel}/P (%)	P_{iW}/P (%)	P_{eW}/P (%)	P_{W}/P (%)	P_{iA}/P (%)	P_{eA}/P (%)	P_{A}/P (%)	η_{ene} $(=P_{\mathrm{P}}/P)$ (%)	η_{div} (%)	η_{disp} (%)	η (%)
D	4.22	13.1	4.2	3.7	7.9	0.8	3.2	4.0	75.0	83.4	83.1	52.0
C-Float	4.18	13.3	4.9	3.3	8.2	0.8	3.2	4.0	74.5	83.7	82.8	51.6
C-Tied	4.19	12.8	3.9	5.3	9.2	1.3	1.4	2.7	75.3	83.6	82.1	51.7

Therefore, their summation surpasses 100%. For the ion current balance, $I_{\mathrm{iC}}/I_{\mathrm{prod}}$ amounts to about just 0.3% among simulated cases, and has been omitted in Tab. 3. The plasma power losses to the thruster walls, P_{W} and P_{A}, have been conveniently split into its corresponding ion and electron contributions, namely: P_{iW} and P_{eW}, and P_{iA} and P_{eA}.

Simulation results show that global performance figures, including F, I_{d}, P, η (refer to Tab. 1), I_{prod} and partial efficiencies in Tabs. 3 and 4 are not significantly affected by the change in the channel wall conditions, and take values not far from those found for SITAEL's HT5k.[10] For all cases here, high values of η_{u} and η_{cur} are found, and the mean half-divergence angle based on energy flows is $\alpha_{\mathrm{div}} = \arccos\sqrt{\eta_{\mathrm{div}}} \approx 24$ deg. As for the HT5k, plasma recombination at the thruster walls is high since almost 60% of the produced ion current is collected there (A + W). However, the total power deposited at the thruster walls is just 11-12%, demonstrating the advantages of the MS topologies.

As anticipated from the analysis of Fig. 6, Cases D and C-Float exhibit a very similar distribution of electron current to walls, while Case C-Tied is significantly different in this regard. In the latter case, there is a deficit (in absolute terms) of around a 34% in $I_{\mathrm{eA}}/I_{\mathrm{prod}}$ with respect to the other two cases, which is compensated by a similar increase (in absolute terms) in $I_{\mathrm{eW}}/I_{\mathrm{prod}}$, confirming the redistribution in the electron current to walls from Cases D and C-Float to Case C-Tied. The terms of the ion current balance $I_{\mathrm{iW}}/I_{\mathrm{prod}}$ and $I_{\mathrm{iA}}/I_{\mathrm{prod}}$, in Tab. 3, vary only slightly from Cases D and C-float to Case C-Tied. These variations in I_{i} ($\sim 3\%$ of I_{prod}) are caused by small changes in the gradients of ϕ, required to redistribute I_{e} among the thruster walls. In Case C-Tied, the fraction of I_{d} that flows through the channel walls, $I_{\mathrm{W}}/I_{\mathrm{d}}$, is approximately 75%. In Ref. 1, experimental observations for the H9C thruster in anode-tied configuration yield $I_{\mathrm{W}}/I_{\mathrm{d}} = 33 - 40\%$. Unlike the VHET-MS, the H9C features a MS topology without $\boldsymbol{B}$ null point inside the thruster chamber.[27] Differences in the magnetic topology (and geometry) could be postulated as one of the main reasons for the disagreement in the fraction of I_{d} collected at the channel conducting walls.

Case C-Tied exhibits a 32.5% relative decrease of the power fraction to the anode wall P_{A}/P with respect to Cases D and C-Float, which is mainly driven by the lower electron current fraction to the anode wall (53-54% relative decrease of $I_{\mathrm{eA}}/I_{\mathrm{prod}}$). Reducing the heat load to the anode can help keeping anode temperature at nominal operating conditions without the need of complex active cooling systems which can pose severe restrictions for practical operation.[28] Since $\eta_{\mathrm{ene}} = P_{\mathrm{P}}/P$ remains approximately the same, the lower P_{A}/P implies higher P_{W}/P in Case C-Tied. Appart from possible advantages due to the extra thermal conductivity obtained from thermally connecting anode and conducting channel walls,[1] this redistribution of the heat loads may be beneficial for thermal management, because thermal paths towards surfaces for radiative heat rejection can be shorter from the channel walls than from the anode (i.e., it is easier to evacuate P_{W} than P_{A}).

VI. Conclusions

This paper presents 2D hybrid fluid-kinetic simulations of a virtual 5 kW MS-HET, in which the material of the channel walls have been switched from dielectric to conducting. Two different electrical configurations have been considered for the conducting channel walls: floating and anode-tied.

Bulk plasma properties and main performance metrics, in agreement with previous experimental works, are only slightly altered when conducting channel walls are considered, instead of dielectric ones. This demonstrate that the MS-HET discharge can operate with conducting channel walls without loss of efficiency. The plasma density, the plasma potential, and the electron temperature remain nearly the same for all cases, exhibiting features typical of an effective MS topology. The magnitude that is mainly affected by the change in the wall material (and electric configuration) is the electron current density within the thruster chamber. Much slighter effects are observed for the current density solution of nearly unmagnetized ions. The case

with conducting channel walls in floating configuration is, in terms of the electron current density map, very similar to the dielectric case, because the total electric current collected by the channel walls is still zero and I_d remains roughly the same for all cases. In particular, both scenarios exhibit the same electron current density and energy flux profiles along the anode wall.

In the scenario with conducting anode-tied channel walls, however, the channel walls collect an electron dominated net current that amounts to 75% of I_d, and a notably different electron current density 2D map is obtained. Main differences are observed upstream the position of the magnetic null point within the chamber, from where electron current is redistributed to the different thruster walls, with minimal changes in the gradients of the electric potential and the plasma density. The redistribution of the electron current to the thruster walls implies a reduction in the electron flux to the anode wall, which, in turn, reduces the power deposited there and increases the heat load to the thruster channel (for the same total input power). This fact presents potential advantages from the thermal management perspective. First, reducing heat loads to the anode can greatly simplify anode thermal design and cooling strategies. Second, redirecting thermal loads to the lateral walls can facilitate radiative heat rejection from the channel. This work shows that it may be possible to achieve optimal distributions of heat loads to the thruster walls in MS-HETs with conducting walls, without significant performance degradation, which can be a key aspect to overcome severe thermal requirements for the development of high power HETs.

Acknowledgments

References

[1] R. Hofer and S. Arestie, "Performance of a conducting wall, magnetically shielded hall thruster at 3000s specific impulse," in *37th International Electric Propulsion Conference*, ser. IEPC-2022-401, 2022.

[2] D. M. Goebel, R. R. Hofer, I. G. Mikellides, I. Katz, J. E. Polk, and B. N. Dotson, "Conducting wall Hall thrusters," *IEEE Transactions on Plasma Science*, vol. 43, no. 1, pp. 118–126, 2015.

[3] L. Su, T. Gill, P. Roberts, W. Hurley, T. Marks, C. Sercel, M. Allen, C. Whittaker, M. Byrne, Z. Brown, E. Viges, and J. B.A., "Operation and performance of a magnetically shielded Hall thruster at ultrahigh current densities on xenon and krypton," in *AIAA SCITECH 2023 Forum*. National Harbor, MD: AIAA, 2023.

[4] L. Grimaud and S. Mazouffre, "Conducting wall Hall thrusters in magnetic shielding and standard configurations," *Journal of Applied Physics*, vol. 122, no. 3, 2017.

[5] L. Grimaud, "Magnetic shielding topology applied to low power Hall thrusters," Ph.D. dissertation, Université d'Orléans, 2018.

[6] L. Grimaud and S. Mazouffre, "Performance comparison between standard and magnetically shielded 200W Hall thrusters with BN-SiO2 and graphite channel walls," *Vacuum*, vol. 155, pp. 514–523, 2018.

[7] D. Pérez-Grande, "Fluid modeling and simulation of the electron population in hall effect thrusters with complex magnetic topologies," Ph.D. dissertation, Universidad Carlos III de Madrid, Leganés, Spain, 2018.

[8] A. Domínguez-Vázquez, "Axisymmetric simulation codes for hall effect thrusters and plasma plumes," Ph.D. dissertation, Universidad Carlos III de Madrid, Leganés, Spain, 2019.

[9] A. Domínguez-Vázquez, J. Zhou, P. Fajardo, and E. Ahedo, "Analysis of the plasma discharge in a Hall thruster via a hybrid 2D code," in 36th *International Electric Propulsion Conference*, no. IEPC-2019-579. Vienna, Austria: Electric Rocket Propulsion Society, 2019.

[10] J. Perales-Díaz, A. Domínguez-Vázquez, P. Fajardo, E. Ahedo, F. Faraji, M. Reza, and T. Andreussi, "Hybrid plasma simulations of a magnetically shielded Hall thruster," *Journal of Applied Physics*, vol. 131, no. 10, p. 103302, 2022.

[11] J. Perales-Díaz, "Fluid-kinetic models for space plasma thrusters," Ph.D. dissertation, Universidad Carlos III de Madrid, Leganés, Spain, 2024.

[12] I. Mikellides, I. Katz, R. Hofer, D. Goebel, K. de Grys, and A. Mathers, "Magnetic shielding of the channel walls in a Hall plasma accelerator," *Physics of Plasmas*, vol. 18, p. 033501, 2011.

[13] J. Zhou, "Modeling and simulation of the plasma discharge in a radiofrequency thruster," Ph.D. dissertation, Universidad Carlos III de Madrid, Leganés, Spain, 2021.

[14] J. Zhou, A. Domínguez-Vázquez, P. Fajardo, and E. Ahedo, "Magnetized fluid electron model within a two-dimensional hybrid simulation code for electrodeless plasma thrusters," *Plasma Sources Science and Technology*, vol. 31, no. 4, p. 045021, 2022.

[15] D. Pérez-Grande, O. González-Martínez, P. Fajardo, and E. Ahedo, "Analysis of the numerical diffusion in anisotropic mediums: benchmarks for magnetic field aligned meshes in space propulsion simulations," *Applied Sciences*, vol. 6, no. 11, p. 354, 2016.

[16] E. Ahedo and V. Pablo, "Combined effects of electron partial thermalization and secondary emission in Hall thruster discharges," *Physics of Plasmas*, vol. 14, p. 083501, 2007.

[17] A. Domínguez-Vázquez, J. Zhou, A. Sevillano-González, P. Fajardo, and E. Ahedo, "Analysis of the electron downstream boundary conditions in a 2D hybrid code for Hall thrusters," in 37th *International Electric Propulsion Conference*, no. IEPC-2022-338. Boston, MA, June 19-23: Electric Rocket Propulsion Society, 2022.

[18] S. Mazouffre, P. Echegut, and M. Dudeck, "A calibrated infrared imaging study on the steady state thermal behaviour of Hall effect thrusters," *Plasma Sources Science and Technology*, vol. 16, no. 1, p. 13, 2006.

[19] I. Mikellides, I. Katz, D. M. Goebel, K. K. Jameson, and J. E. Polk, "Wear mechanisms in electron sources for ion propulsion, 2: Discharge hollow cathode," *Journal of Propulsion and Power*, vol. 24, no. 4, pp. 866–879, 2008.

[20] Biagi, S.F., "Cross sections extracted from PROGRAM MAGBOLTZ, version 7.1 june 2004," June 2004, [Online; accessed 5-July-2021]. [Online]. Available: www.lxcat.net/Biagi-v7.1

[21] M. Mitchner and C. Kruger Jr., *Partially ionized gases.* John Wiley and Sons, Hoboken, NJ, 1973.

[22] A. Domínguez-Vázquez, F. Cichocki, M. Merino, P. Fajardo, and E. Ahedo, "On heavy particle-wall interaction in axisymmetric plasma discharges," *Plasma Sources Science and Technology*, vol. 30, no. 8, p. 085004, aug 2021.

[23] S. Araki and R. Wirz, "Magnetic field aligned mesh for ring-cusp discharge chambers," in *50th AIAA/ASME/SAE/ASEE Joint Propulsion Conference & Exhibit*, no. AIAA 2014-3830, Cleveland, Ohio, US, 2014.

[24] I. G. Mikellides, I. Katz, R. R. Hofer, and D. M. Goebel, "Magnetic shielding of a laboratory Hall thruster. I. theory and validation," *Journal of Applied Physics*, vol. 115, no. 4, p. 043303, 2014.

[25] I. G. Mikellides, R. R. Hofer, I. Katz, and D. M. Goebel, "Magnetic shielding of Hall thrusters at high discharge voltages," *Journal of Applied Physics*, vol. 116, p. 053302, 2014.

[26] N. P. Brown and M. L. R. Walker, "Review of plasma-induced hall thruster erosion review of plasma-induced hall thruster erosion," *Applied Sciences*, vol. 10, no. 11, p. 3775, 2020.

[27] R. Hofer, S. Cusson, R. Lobbia, and A. Gallimore, "The H9 Magnetically Shielded Hall Thruster," in *35th International Electric Propulsion Conference*, ser. IEPC-2017-232, 2017.

[28] C. Book and M. Walker, "Effect of anode temperature on Hall thruster performance," *Journal of Propulsion and Power*, vol. 26, no. 5, 2010.